Nanohoneycomb rGO Foam as a Promising Anode Material for Unprecedented Ultrahigh Li Storage and Excellent Endurance at Ampere Current Stability

Abu Talha Aqueel Ahmed,[1] Akbar I. Inamdar,[1] Bo Hou,[2] S. Cho,[1] Chan-Cuk Hwang,[3] Docheon Ahn,[3] Jung Inn Sohn, *[1] SeungNam Cha,*[4] Hyungsang Kim,[1] Hyunsik Im*[1]

[1]*Division of Physics and Semiconductor Science, Dongguk University, Seoul 04620, Republic of Korea.*
[2]*School of Physics and Astronomy, Cardiff University, Cardiff, Wales CF24 3AA, United Kingdom*
[3]*Beamline Department, Pohang Accelerator Laboratory, Pohang, Gyeongbuk 37673, Republic of Korea*
[4]*Department of Physics, Sungkyunkwan University, Suwon, Gyeonggi-do 16419, Republic of Korea*

* Author to whom correspondence should be addressed.

E–mail: junginn.sohn@dongguk.edu, chasn@skku.edu, hyunsik7@dongguk.edu

Abstract

Most rechargeable lithium-ion batteries (LIBs) exploit bulk carbon (e.g., graphite with low interlayer spacing of 0.335 nm) as an anode material despite its low theoretical capacity of 372 mAh g^{-1} because it has a high coulombic efficiency, good cycling performance, and low production costs. However, it is difficult to increase the specific capacity of graphite-based anodes without sacrificing these inherent advantages. In the present study, we developed reduced graphene oxide nanohoneycomb foam (H-rGO) as an anode material with higher surface area, porosity, and interlayer spacing for the rapid and efficient lithiation-delithiation of Li-ions. The combination of the hierarchical three-dimensional sponge-like mesoporous structure with highly efficient Li-ion conduction pathways and enlarge active surface area leads to a significantly improved specific capacity (1031 mAh g^{-1} at 0.1 A g^{-1}) and rapid charging with exceptional stability over 5,000 cycles. The H-rGO anode achieves an outstanding reversible capacity of ~534 mAh g^{-1} over 2,500 cycles at 1.0 A g^{-1}, with a capacity retention of 87 and 84% at high current densities of 10 and 20 A g^{-1}, respectively. Our approach is fully compatible with current LIBs technology and offer a simple and efficient strategy to significantly

increase Li-storage capacity of under current graphite-based anode technology.

Keywords: rGO; Graphene nanohoneycomb sponge; Li-ion battery; controlled morphology tinning; fast charging anode

1. Introduction

Since their emergence in the 1970s, the demand for rechargeable high–energy lithium–ion batteries (LIBs) has continued to grow [1-3]. Currently, LIBs dominate the market for many applications, including portable devices, electrical vehicles, and aerospace and military technologies [4-6]. Even though it possesses a low theoretical maximum capacity of 372 mAh g^{-1}, graphite is widely used as an anode in conventional LIB systems because it offers several unique advantages, including a low electrochemical potential for reversible Li–ion storage and release, long–term stability, and low production costs [7-9]. However, the graphite anode experiences the deposition of Li-metal at high charging rates. Significant advances in the power density, energy density, cycle life, rapid charging, and high-rate operation of LIBs are required to ensure their continued success while maintaining their safety and low production costs. Therefore, to reduce the internal resistance and to optimize the trade-off between rapid charging and energy density, a significant effort has been devoted to the development of alternative graphite/graphene–based carbonaceous anode materials with an excellent Li–ion storage capacity, a high energy density, rapid lithiation–delithiation, and ultra–long–term cyclic stability [10, 11].

Graphene, which is characterized by a two–dimensional honeycomb lattice consisting of sp^2–hybridised carbon monolayer, has attracted significant attention due to its beneficial geometrical and intrinsic physical properties, such as its large theoretical specific surface area (~ 2600 $m^2\ g^{-1}$), robust intrinsic mechanical strength (42 N m^{-1}), good transparency, high charge mobility (2×10^5 $cm_2\ Vs^{-1}$), and broad electrochemical window. It also offers exceptional functional properties such as high heat and electrical conductivity (~ 2000 S cm^{-1}) [11-15]. In 1995, Dahn *et al.* proposed that a single graphene layer can host twice as many Li–ions as the conventional graphite anode (by utilizing both sides of the graphene layer). This is possible because the graphene layers forms intercalated Li_2C_6 rather than LiC_6, thus leading to a specific capacity that is twice compared to conventional commercialised graphite anodes [16-18]. However, despite the low material density (~ 0.01 g cm^{-3}) and high specific surface area of monolayered graphene, it does not have a high volumetric energy density due to the low occupancy of Li–ions as a result of thermodynamically unfavourable Li–ion storage, thus leading to a low coulombic efficiency [11, 19, 20].

To date, several research groups have proposed various few–layer graphene–based and graphene–incorporated battery anodes with improved specific capacities and

cycling stability at low current densities (≤ 0.1 Ag^{-1}), such as graphene nanoballs, graphene–like graphite, carbon nanotube–derived graphene, nitrogen–incorporated graphen oxide (N–GO), and reduced graphen oxide (rGO) [13, 19, 21-23]. The development of graphene–based anodes has been effective, as the graphene is used to modify Si and Ge anodes to prevent volumetric expansion, and also it acts as a cushion to buffer the volume change during the lithiation–delithiation in the SnS_2/NRGO composite [22, 24, 25]. Son et al. examines the use of graphene anode with graphene–coated cathode that can lead to a high volumetric energy density with a high–capacity retention rate of 78.6% after 500 cycles [26]. Liu et al. demonstrate that graphene–modulated V_2O_5 can achieve excellent LIB performance with a specific capacity of 438 mAh g^{-1} [27]. Further, compositing metal with graphene or forming core-shell heterostructure has also been demonstrated as a highly promising anode for LIBs [28-32]. However, these anodes exhibit an unsatisfactory Li–ion storage capacity in the high current density region (≥ 10 Ag^{-1}) because of the deformed material structure caused by the rapid lithiation–delithiation, which restricts charge transport, reduces the capacity, and leads to poor cyclabilities [12, 33-36]. Other difficulties associated with viable use of these materials include complex manufacturing, high production costs, and the non–uniformity of the electrode material. Therefore, new chemical strategies are required to overcome these technical barriers and improve the energy and power capacity of the resulting anode material.

Herein, we report a new structural network design concept for the disassembly and reconstruction of bulk graphite at the nanoscale level. This involves disassembling graphite into GO and using this to create a nanohoneycomb sponge–like rGO (H-rGO) structure (**Fig. 1**). The H–rGO architecture provides an ideal morphology for the efficient reversible lithiation–delithiation of Li–ions, resulting in a high reversible capacity of 1031 mAh g^{-1} at 0.1 A g^{-1}, excellent restoration (~ 94% at 0.1 A g^{-1}), and good retention capacity (~ 117% at 1.0 A g^{-1} after 500 cycles), which greatly exceeds the theoretical capacity of graphite and pure carbon–based anode materials recently reported in the literature. The H-rGO anode exhibits an outstanding Li–ion storage capacity at various current densities (1−20 A g^{-1}) and temperature ranges (−5 °C to 55 °C), and it displays good capacity endurance over 5,000 lithiation–delithiation cycles.

2. Experimental section

2.1 H–rGO synthesis

Self–assembled H-rGO was prepared by reconstructing disassembled GO nanosheets at the nanoscale level (**Fig. 1**). First, GO nanosheets were synthesised from natural graphite (NG) using a modified Hummers method [37, 38]. Details of the experimental synthesis process are provided in the supporting experimental section. In the typical procedure, NG was dispersed in a sulfuric acid (H_2SO_4) solution under vigorous stirring in an ice bath, and then a potassium permanganate ($KMnO_4$, GR grade) solution was added dropwise. The suspension was transferred to a shaking

incubator for the oxidation of the graphite surface and edges. The GO sheets were exfoliated from the oxidised graphite with the dropwise addition of de–ionised (DI) water and subsequent mixing of the sheets with hydrogen peroxide (H_2O_2). The GO solution was filtered and washed through centrifugation. Pure GO nanosheets were obtained after ageing the precipitate in a microporous membrane tube. To obtain H–rGO, excess quaternary ammonium salt (QAS) was added to the GO solution under continuous stirring for about 1 h. The reaction rapidly occurred under stirring and a GO–QAS composite (S-GO) was promptly synthesised within several minutes. The functional groups on GO nanosheets generally exhibit good reactivity with QAS, thus a nanohoneycomb–like structure formed after the reduction process in a similar manner to a self–assembly. The solution mixture was then washed several times with DI water and filtered using filter paper. The GO–QAS composite clay was dissolved in DI water and lyophilised in a freeze–dryer (LP–10; IlsinBioBase Co., Ltd.) overnight. Finally, H-rGO was obtained by thermally treating the GO–QAS powder at 1000 °C under a flow of N_2 gas (3 L min^{-1}) in a quartz tube.

2.2 Materials characterizations

High–resolution synchrotron powder X–ray diffraction (HR–XRD) data for the NG, GO, rGO, and H-rGO powder samples were obtained from the 9B beamline of PLS–II. The incident X–rays (beam size of 20 × 1 mm^2 at the sample position) were vertically collimated using a mirror and monochromatised to a wavelength of 1.5167 Å with a double–crystal Si (111) monochromator. The detector arm of the vertical scan diffractometer comprised seven sets of Soller slits, flat Ge (111) crystal analysers, anti–scatter baffles, and scintillation detectors, with each set separated by 20°.

The topographical modification and compositional properties of the NG, GO, rGO, and H-rGO samples were examined using field–emission scanning–electron microscopy (FESEM) and energy dispersive X–ray spectroscopy (EDS), respectively, using a JSM–6701F microscope that was operated at 15 kV. Furthermore, the microstructural properties of the proposed rGO and H-rGO samples were characterised using transmission electron microscopy (TEM), high–resolution TEM (HRTEM), and selected–area electron diffraction (SAED) with a JEOL–3000F microscope operating at an accelerating voltage of 300 kV with a camera length of 255.8 mm. The morphology and chemical composition of the samples were also investigated using scanning TEM–bright field (STEM–BF) and STEM–high angle annular dark field (STEM–HAADF) analysis, respectively, with a Cryo cartridge holder.

The N_2 adsorption–desorption isotherms of the prepared samples were measured (ASAP 2020, Micromeritics) at 77 K to compare their specific surface area and pore–diameter distributions. The specific surface area for each sample was calculated using the Brunauer–Emmett–Teller (BET) adsorption isotherm theory based on the following equations:

$$\left[\frac{1}{V_a\left[\frac{P_0}{P}-1\right]}=\frac{C-1}{V_mC}\times\frac{P}{P_0}+\frac{1}{V_mC}\right]$$

where P is the partial vapour pressure of the nitrogen gas adsorbate in equilibrium with the surface at 77.4 K, P_0 is the saturated pressure of nitrogen gas adsorbate, V_a is the volume of gas adsorbed at standard temperature and pressure (STP), V_m is volume of gas adsorbed at STP to produce an apparent monolayer on the sample surface, and C is a dimensionless constant that is related to the enthalpy of adsorption of the nitrogen gas adsorbate on the sample.

$$S=\frac{V_m\times N\times a}{m\times 22400}$$

where A is the specific surface area, N is the Avogadro constant, a is the effective cross-sectional area of one adsorbate molecule (0.162 nm^2 for nitrogen), and m is the mass of the sample.

In the high–resolution photoemission spectroscopy (HRPES) experiments, the rGO and H–rGO powders were mounted on a Mo plate with an Au sheet to calibrate their photon energy. All photoemission data were collected using a Scienta R4000 electron analyser from the 10D beamline at Pohang Accelerator Laboratory under a pressure of 1.0×10^{-10} Torr. The wide survey spectra and O 1s spectra were obtained using a photon energy of 630 eV, whereas the C 1s and N 1s spectra were obtained using photon energies of 360 and 500 eV, respectively. This was because the N 1s peak was barely visible in the spectra recorded at 630 eV but became visible as the photon energy decreased to 500 eV due to the enhanced photoionisation cross–section.

2.3 Electrode and half–cell anode fabrication

The battery performance of the anode samples was examined using CR2032 coin–type cells in a half–cell configuration. LIB anode electrode films were fabricated using a doctor blade technique. A coating slurry was prepared by mixing 80 wt.% active material (NG, GO, rGO, or H-rGO), 10 wt.% carbon black, 10 wt.% polyvinylidene fluoride, and N–methyl 1–pyrrolidone to achieve the required consistency. The mixed slurry was then cast on copper foil as a current collector and the coated film was vacuum–dried in an oven at 60 °C. A 15 mm diameter section of the current collector was punched out and used as the working electrode. The loading weight of the active material on the current collector for NG, GO, S-GO, rGO, and H-rGO were 3.92, 3.22, 3.04, 1.32, and 1.46 mg, respectively. Celgard 2400 and a Li–metal foil disk (19 mm) was used as the separator and counter electrode, respectively. The coin–type cell was assembled in an argon–filled glove box (Korea Kiyon) [39, 40]. A 1.0 M $LiPF_6$ electrolyte was used consisting of a mixture of ethylene carbonate and diethyl carbon (EC/DEC; 1:1 v/v). Lithiation–delithiation and cyclic voltammetry (CV) tests were

conducted in a voltage range of 0.005–3.000 V (*vs* Li/Li^+) using a Bio–logic instrument (France). The discharge/charge cyclability of the anode cell was galvanostatically investigated at various current densities, and the CV measurements were conducted at various scan rates. Electrochemical impedance spectroscopy (EIS) measurements were recorded over a frequency range of 0.005–20.000 kHz.

3. Results and Discussion

Figure 2a shows the HR–XRD patterns of NG, GO, rGO, and H-rGO. The characteristic (002) diffraction peak of GO is observed at $2\Theta = 11.26°$ indicating that the distance between the GO layers is 7.8 Å. The distance between the GO layers is higher than the (002) spacing (~ 3.36 Å) of graphite because of the introduction of multiple oxygen–containing groups at the edge of each layer. The HR–XRD pattern of the surfactant–mediated GO (S-GO), which was used to form the nanohoneycomb–like structure after thermal reduction, was also recorded (**Fig. S1a**) for comparison with that of pristine GO. The (002) spacing of S-GO intercalated with the nitrogen–based surfactant increase to 9.7 Å ($2\Theta = 9.12°$), considerably higher than that of pristine GO. It is therefore evident that the S-GO interlayer contains different functional groups from those found in GO.

The rGO and H-rGO samples that were obtained after the reduction of GO and S-GO, respectively, exhibits (002) and (100) diffraction peaks typical of rGO (JCPDS card no. 75−1621). The (002) peak profiles of rGO and H-rGO were fitted using the Pearson VII function, and the fullwidth at half–maximum (FWHM) at the (002) peak position was obtained to quantitively analyse their structure. The average crystallite size of rGO and H-rGO in the *c*–direction was estimated using the Scherrer equation ($L = 0.94\,\lambda/\beta(\Theta)\cos 2\Theta$, where L is the crystallite size, λ is the X–ray wavelength, $\beta(\Theta)$ is the FWHM at Θ, and Θ is the Bragg diffraction angle) [41]. It is well known that the L (002) for a graphene system is equal to the average height (i.e., thickness) of the stacked rGO layers, with a graphene monolayer typically having a thickness of about 3.45 Å. The structural analysis reveals that the rGO and H-rGO samples consists of approximately six and four graphene layers, respectively (**Table 1**). Furthermore, rGO has a shorter (002) lattice plane spacing between its graphene layers than H-rGO. This could be due to H-rGO having a higher degree of reduction than rGO.

Table 1. Fitted FWHM at the (002) peak position and structural information for the rGO and H-rGO samples.

Sample	(002) Peak

	FWHM[a] (°)	2Θ[a] (°)	L[b] (Å)	d[c] (Å)
rGO	5.88	25.99	20	3.4
H-rGO	4.00	25.15	14	3.5

[a] Values fitted using the Pearson VII function, [b] average height (thickness) of the stacked graphene layers, and [c] average distance between the graphene layers.

The morphologies of the graphene sheets from bulk carbon to a few layers and/or the nanohoneycomb–like structure were examined using FESEM image analysis. **Figs. 2b–d** show the obtained FESEM images of NG, GO, rGO, and H-rGO. Prior to discussing the proposed surfactant–mediated rGO and non–surfactant–mediated rGO, it must be highlighted that the as–obtained NG sample (i.e., the primary raw graphite source; **Fig. 2b**) consist of a thick slab of parallel layers of carbon. The pristine GO (**Fig. 2c**) prepared using the traditionally modified Hummers method has a crumpled silk veil–like structure composed of compressed stacked graphene nanoplatelets. These layered nanoplatelets shows the thick wrinkled edges with a few graphene layers lifting from the nanoplatelet surface because of the exfoliation process. The morphologies of both the pristine GO and S-GO are almost identical (**Figs. 2c,S1b**). However, the morphology of GO and S-GO was altered drastically after the thermal reduction process. The rGO sample obtained from the pristine GO consists of corrugated graphene nanosheets with folded edges that has a thickness of several nanometres. Whereas, the H-rGO sample obtained from S-GO was characterized by the self–assembly of graphene nanosheets to forms a nanohoneycomb–like structure due to the interaction of the surface functional groups with the surfactant at the atomic scale. This results in an elevated porous architecture, which is beneficial for an efficient Li–ion storage capacity, and is further discussed in a section below by the Brunauer–Emmett–Teller (BET) results (**Figs. 4a-c**).

The microstructural properties of the rGO and H-rGO structures were systematically studied using TEM, HRTEM, and STEM–HAADF (**Figs. 3,S3**). The results reveal the concurrence of graphite and graphene phases. The TEM image (**Fig. 3a**) shows that H-rGO has a typical interconnected corrugated layered morphology, which is consistent with the FESEM image of H-rGO (**Fig. 2d** inset). The TEM image also reveals the coexistence of allotropic graphite and graphene layers at the convergence/divergence regions of the cell marked with an arrow, forming a hollow space at the right angle (indicated by the light grey region). The hollow architecture increases the porosity (**Fig. S2**) of the nanohoneycomb–like structure compared with that of the pristine rGO, suggesting that H-rGO is likely to demonstrate expeditious

lithiation–delithiation capabilities. The traces of graphite in the nanohoneycomb–like structure are noticeable because a number of graphene layers are integrated in the convergence region. This analysis is supported by HRTEM image analysis (**Fig. 3b**). The locally oriented lattice fringes (outlined by the white and yellow boxes) and lattice distance were identified with d–spacing values of 3.4 ± 1 Å and 2.1 ± 1 Å indexed to the {002} and {100} planes of the graphite phase, respectively, whereas the d–spacing values of 3.2 ± 1 and 7.1 ± 1 Å originated from the {222} and {111} planes of graphene, respectively. The coexistence of the graphite and graphene phases was further confirmed by the SAED patterns (**Fig. 3c**). The SAED rings are very broad, and only graphite ((002) and (102)) and graphene ((420), (311), and (200)) reflections are identified with a high degree of confidence [42]. STEM–HAADF elemental line scanning and mapping (**Figs. 3d-f**) provide additional support of the homogeneity of the constituent elements on an atomic scale, while the line–scan data verified that GO was reduced homogeneously without phase or element segregation.

The textural characteristics of NG, rGO, and H-rGO samples was examined using N_2 sorption isotherms based on BET measurements. **Figure 4a** shows the N_2 adsorption−desorption isotherms of the rGO and H-rGO samples. For comparison, a similar isotherm curve for the as–obtained NG is presented in **Fig. S2a**. The standard multi-point BET (**Fig. 4b,S2b**) was used to estimate the specific surface area and the desorption branch of BJH method was used to investigate the pore-size distribution for all of the powder materials. The rGO and H-rGO exhibit type–IV isotherms, indicating the presence of mesopores/micropores, and further display H3 isotherm hysteresis loops, indicating that a slit–like porous architecture formed as a result of the interlayer spacing between the graphene layers and/or the self–assembled nanohoneycomb–like structure forming stable voids [43, 44]. The NG, rGO, and H-rGO samples exhibits the BET surface areas of 2.54, ~ 769, and 441 $m^2 g^{-1}$ and average pore diameters of ~ 14, 8, and 13 nm, respectively (**Figs. 4a,c**). The variation in the BET surface area is ascribed primarily to the different geometries and topographies of NG, rGO, and H-rGO observed in the FESEM analysis (**Figs. 2b-e**). In particular, the rGO sample has a higher BET surface area than the H-rGO sample indicating that it had a considerably wavier graphene nanosheet structure. This analysis is further supported by the corresponding FESEM images (**Figs. 2d,e**). Notably, the BET surface area for the rGO and H-rGO samples is considerably lower than for the single layer graphene (2600 $m^2 g^{-1}$), which is due to the multilayer stacking of the graphene nanosheets in the rGO and H-rGO structures, as evidenced from the XRD analysis (**Fig. 2a**) [45]. Nonetheless, H-rGO has a larger BET pore–size distribution than rGO, which may be associated with its unique honeycomb–like morphology that resulted from surfactant–mediated synthesis strategy. This unique morphology provides a sufficient electrolyte contact interface and favourable ion diffusion paths. Consequently, our unique nanoscale nanohoneycomb–like structure has the potential to demonstrate greater electrochemical capacity and improved charge transfer kinetics.

The elemental configuration and binding states of the constituent elements were analysed using HRPES analysis. **Figure 5** shows the HRPES spectra of rGO and H–

rGO, with the characteristic O–related and C–related peaks are dominant. Notably, rGO exhibits no nitrogen trace in its N 1s spectrum. However, H-rGO shows an additional N 1s emission peak (**Fig. 5a**) that originated from the pyridinic (N1), pyrrolic (N2), graphitic (N3), and oxidized (N4) nitrogen species. The presence of these N species in the H-rGO structure is associated to the nitrogen atoms of the surfactant used during the synthesis of S-GO; these nitrogen atoms were incorporated into the H-rGO structure during the reduction process, leading to the appearance of C 1s and O 1s spectral features that are distinct from those exhibited by rGO. **Figure 5b** shows the C 1s spectra of rGO and H-rGO, which mainly consist of four components: C1 (~ 284.5 eV), C2 (~ 285 eV), C3 (~ 286 eV), and C4 (~ 289 eV) [16-18, 46-52]. Both rGO and H-rGO exhibits the characteristic C1 and C2 components related to the C–C and C=C bonds, respectively, in the graphene nanosheets, accounting for over 80% of the carbon constituent in the C 1s spectrum. The remaining C3 and C4 components are ascribed to the C–O or C–N bonds, which account for less than 20% of the C 1s signal. For rGO (without nitrogen), the C3 and C4 components should correspond to the C–O–C or C–OH and C=O bonds, respectively, which are typically found in rGO [52]. Conversely, the C3 and C4 components in H-rGO are expected to additionally indicate the presence of C–N (C3) and C=N–C–O (C4) [46].

The O 1s spectra (**Fig. 5c**) of rGO and H-rGO exhibits three characteristic components: O1 (~ 533 eV; C–O–C), O2 (~ 532 eV; C–OH), and O3 (~ 531 eV; C=O) [17, 49, 53-58]. The O1 and O2 components accounted for over 90% of the total intensity, which is consistent with the dominance of C3 component in the C 1s spectrum. Similarly, the relatively low contribution of the O3 component is consistent with the infinitesimally small C4 component (< 1%) in the C 1s spectrum. Unlike rGO, the O 1s spectrum for H-rGO exhibits a weak and long tail at ~ 530 eV, which corresponds to the O4 component arising from C=N–C–O [55, 58, 59]. The O4 component and the N 1s peak strongly support the presence of nitrogen atoms in the H-rGO sample. Moreover, rGO has more oxygen between its graphene layers than H-rGO. The HRPES analysis confirms that C1s and O 1s core levels are present in the spectra without any trace of impurities and that N 1s was successfully attached to the nanohoneycomb–like structure.

Figure 6 displays the electrochemical properties of H-rGO as an LIB anode. The CV curves were recorded to survey the LIB performance of the anodes at a scan rate of 0.1 mV s^{-1}. **Figure 6a** shows the initial five CV sweeps for H-rGO. The comparative CV curves for NG, GO, and rGO were also recorded under the same experimental conditions (**Fig. S4**). The H-rGO anode has a higher area under the CV curve than the NG, GO, and rGO anodes, suggesting that H-rGO could store more Li–ions. The H-rGO anode exhibits one broad and intense peak ranging between 1.02 and 0.4 V (*vs* Li/Li^+), which is associated with the formation of an SEI layer, and two weak peaks at 0.22 and 0.13 V (*vs* Li/Li^+). The broad peak disappears in subsequent cycles, whereas both peaks (0.22 and 0.13 V (*vs* Li/Li^+)), which were originated from the lithiation process, remained in each cathodic sweep. Conversely, two oxidation peaks are observed at about 0.34 V and 1.25 V (*vs* Li/Li^+) during the anodic sweep. An oxidation peak

emerged at 0.34 V (*vs* Li/Li^+) is an indicative of maximum Li^+ insertion [47]. Whereas the well–developed peak at ~1.25 V (*vs* Li/Li^+) could be attributed to the breaking of the Li atomic bonds between active sites or defect states during charging state, arising from the interaction between the relatively strong Li bonds and functional groups containing residual nitrogen within the graphene nanosheets [46, 53]. The consistent intensity of the oxidation/reduction peaks during the consecutive sweeps suggests that H-rGO has excellent reversibility during anodic/cathodic scans.

The galvanostatic discharge/charge characteristics of the H-rGO anode recorded at a steady current of 0.1 A g^{-1} and are presented in **Fig. 6b**, while the similar discharge/charge properties of NG, GO, and rGO anodes are portrayed in **Fig. S5**. The H-rGO anode exhibits two plateaus in the first discharge curve. The first plateau at ~ 0.65 V (*vs* Li/Li^+) is attributed to the formation of an SEI layer on the graphene surface, the decomposition of the electrolyte, and the simultaneous formation of organic Li compounds. The second plateau in the low–potential region (< 0.4 V (*vs* Li/Li^+)) is due to the lithiation peaks (0.22 and 0.13 V (*vs* Li/Li^+)). Therefore, the observed capacity at ≤ 0.4 V (*vs* Li/Li^+) is mainly attributed to the Li^+ intercalation process, whereas the capacity in the high–potential region is attributed to the side reaction (i.e., SEI layer formation) or faradaic capacitance [54, 55, 59]. The total discharge capacity of H-rGO in the first discharge reaches to 2287 mAh g^{-1}, which is much higher than the theoretical capacity of graphite (372 mAh g^{-1}) and the estimated specific capacity of the rGO anode (1579 mAh g^{-1}). However, a recovery of only 1039 and 990 mAh g^{-1} was observed for rGO and H-rGO, respectively, while extracting two Li–ions after the first full charge (**Fig. 6c**). Thereafter, the discharge capacity of rGO and H-rGO decrease further to 778 and 1031 mAh g^{-1}, respectively, which is ascribed to the formation of the SEI layer on the graphene surface. The H-rGO anode exhibits more stable discharge/charge properties in subsequent cycles (**Fig. 6b**) than the rGO anode (**Fig. S5c**), indicating that the loss of capacity with succeeding cycles in the rGO may have been due to the destruction of the intercalated channels for the Li–ions [60].

The clear difference in the lithiation–delithiation performance of the rGO and H-rGO anodes is highlighted in **Fig. 6d**, which shows their restoration capacity at various current densities to clarify reversible Li–ion storage mechanisms of the anodes. When the current density increased from 0.1 to 5.0 A g^{-1}, all of the anodes demonstrated a non–linear loss of capacity. The H-rGO anode has a higher Li–ion storage capacity than the other carbonaceous anodes at each current density, and it exhibits excellent capacity restoration and coulombic efficiency (≈ 100%) when the current density returned to 0.1 A g^{-1}. In particular, the H-rGO anode delivers a discharge capacity of 1031, 837, 613, 496, 397, and 299 mAh g^{-1} at a current density of 0.1, 0.2, 0.5, 1.0, 2.0, and 5.0 A g^{-1}, respectively, whereas the rGO anode exhibits a discharge capacity of 778, 572, 421, 315, 237, and 153 mAh g^{-1} at the same current densities, respectively. NG also shows a capacity restoration of ~ 100% (**Fig. S6a**), which is why graphite–based materials are used as anodes in commercial LIBs. However, their poor capacity reduces their durability in multifunctional electronic applications. In the present study, it is believed that the superior restoration capability of H-rGO is due to its stable nanohoneycomb

architecture, with a wide pore diameter of 13 nm (compared with 8 nm for rGO), and the increased conductivity with N content, which allows the efficient Li–ion transport at both low and high current densities [61].

Figure 6e shows a schematic diagram of the proposed Li–ion transport mechanisms during the lithiation–delithiation process in a half–cell LIB structure. During the charging state, the Li–ions move from the lithium reservoir (i.e., the cathode) to the anode through a porous membrane (i.e., the separator). The Li–ions are stored at electrochemically and/or geometrically favourable Li–ion active sites on both sides of a single layer, where they react with defects, drip to the surface or edges of the porous honeycomb structure, and are deposited as multiple layers or are intercalate inside the thick stacked graphite layers [62-64]. Conversely, during the discharging process, all the stored Li–ions are extracted from the anode and move towards the cathode. If the diffused Li–ions cannot be retrieved from the stacked graphene layers of the anode, then the discharge/charge storage tends to exhibit fading behaviour.

The change in the specific capacity over multiple cycles was evaluated under specified lithiation–delithiation conditions (**Figs. 7a-c**). **Figure 7a** shows the comparative cycling stability of the rGO and H-rGO anodes measured at a high current density of 1.0 A g^{-1} for 500 cycles. The capacity of the rGO anode immediately decreased during the initial few lithiation–delithiation cycles and then gradually declined for the remaining cycles, which may be due to the instability of the graphene structure. Low– and high–magnification FESEM images recorded after stability testing (**Figs. S7a,b**) revealed that the rGO nanosheets transformed into thick graphite–like slabs. This deformation in the material may be due to the rapid and continuous lithiation-delithiation cycling. However, the specific capacity of the H-rGO anode gradually increased to 506 mAh g^{-1} after about 200 cycles and then remained stable, which might be due to its almost unruptured morphology (**Figs. S7c,d**). The increase in the Li–ion storage capacity could be due to the expansion of the interlayers and/or the further reduction of H-rGO with continuous cycling, thus decreasing the charge transfer resistance (Rct; from 12.53 Ω to 10.66 Ω; Table S1) [60]. The rGO and H-rGO anodes retained 39% and ~ 117% of their specific capacity and exhibits coulombic efficiency of about 90% and 101%, respectively. The excellent specific capacity retention of the H-rGO anode is due to its conductive and stable nanohoneycomb network with a porous architecture, which facilitates efficient Li–ion transportation through the channel, as evidenced from the EIS curves (**Fig. S8**) revealing the lowest Rct for H-rGO.

In addition, the systematic capacity endurance performance of the H-rGO anode was examined at various current densities. **Figure 7b** shows the endurance capability of the H-rGO anode at moderate and high current densities, which produces a satisfactory retention performance of ~ 117%, 98%, 97%, and 93% after 500 cycles at applied current densities of 1, 5, 10, and 20 A g^{-1}, respectively. Even after 5,000 combined lithiation–delithiation cycles at 10 and 20 A g^{-1}, the H-rGO anode maintained its performance (**Fig. 7c**) and demonstrates an excellent capacity endurance of 87% and 84% at very high current densities of 10 and 20 A g^{-1}, respectively.

A comprehensive temperature–dependent lithiation–delithiation analysis was also conducted to understand the accommodative cycling performance of the anode. **Figure 7d** shows the long–term stability performance of the H-rGO anode at a high current density of 10 A g^{-1} as a function of the operating temperature. The H-rGO anode has a specific discharge capacity of ~ 130, 229, and 356 mAh g^{-1} at an operating temperature of −5 °C, 25 °C, and 55 °C, respectively. The Li–ion storage capability was significantly poorer (~ 50%) at the negative operating temperature ambient (at −5 °C) compared to the normal ambient temperature (25 °C). Low or negative operating temperatures can result in high polarisation, which limit the diffusivity of Li–ions in the anode material, increases the charge–transfer resistance, and reduces the ionic conductivity of the electrolyte [65-67]. Conversely, the specific capacity increases as the operating temperature rises to 55 °C, but it exhibits a fading trend during consecutive cycles. This could be due to the decomposition of the anode/electrolyte material, an increase in the side reaction rates, and the heterogeneity of the SEI film [66, 68]. Nonetheless, the reliability of the H-rGO anode is confirmed by evaluating the performance of a set of similar anodes, and the obtained results confirms that its Li–ion storage and capacity retentions are within an acceptable range for long–term cycling (**Fig. S9**).

4. Conclusions

In summary, we synthesised a unique graphene nanohoneycomb structure by systematically disassembling bulk graphite into GO and rGO. FESEM, TEM, and BET analyses revealed that the H-rGO sample maintained a certain degree of graphite/graphene–layered morphology at the convergence/divergence regions of the honeycomb cell, which resulted in an enhanced porous architecture. Furthermore, HR–XRD analysis revealed that H-rGO had a substantially higher interlayer spacing of the (002) plane reflection than rGO, which facilitated the transport of Li–ions through its wide channels. The H-rGO anode exhibited a remarkable reversible Li–ion storage capacity of 1031 mAh g^{-1} at 0.1 A g^{-1}, which is significantly higher than that of rGO (778 mAh g^{-1}) at the same current density. Long–term lithiation–delithiation cycling tests confirmed that the H-rGO anode had a capacity retention of ~ 117% at 1.0 A g^{-1} after 500 cycles, whereas the rGO anode exhibited a capacity retention of only 39% due to the instability of its graphene structure. The H-rGO anode also demonstrated excellent restoration and retention capabilities at various applied current densities and operating temperatures. The excellent electrochemical storage performance of the H-rGO anode was attributed to the stable nanohoneycomb–like structure of the reduced graphene sheets, which formed a highly porous and conductive network. Moreover, the mesopores provided efficient transport pathways for Li–ion diffusion deep into the stacked graphene layers, which resulted in a high restoration capacity and enhanced cycling stability.

CRediT authorship contribution statement

H. Im: Planned the experimental designed and wrote the manuscript with feedback from all the authors. **A. T. A. Ahmed:** Fabricated the samples, performed measurement, data analysis, and wrote the manuscript. **A. I. Inamdar and B. Hou:** Contributed to the data analysis. **C. C Hwang, J. I. Sohn, and D. Ahn:** Participated in experimental discussions and data analysis. **J. I. Sohn:** Discussion and feedback.

Conflicts of interest

There are no conflicts to declare.

Declaration of competing interest

The authors declare that they have no known competing financial interests or personal relationships that could have appeared to influence the work reported in this paper.

Acknowledgments

This work was supported by the National Research Foundation of Korea (2022R1F1A070724, 2021R1A4A5031805, 2021R1A2B5B01001796, 2022M3H4A1A040964).

Appendix A. Supporting data

Supplementary Information is available in the online version and can be found at https://doi.org/xx.xxxx/j.apsusc.2022.xxxxxx.

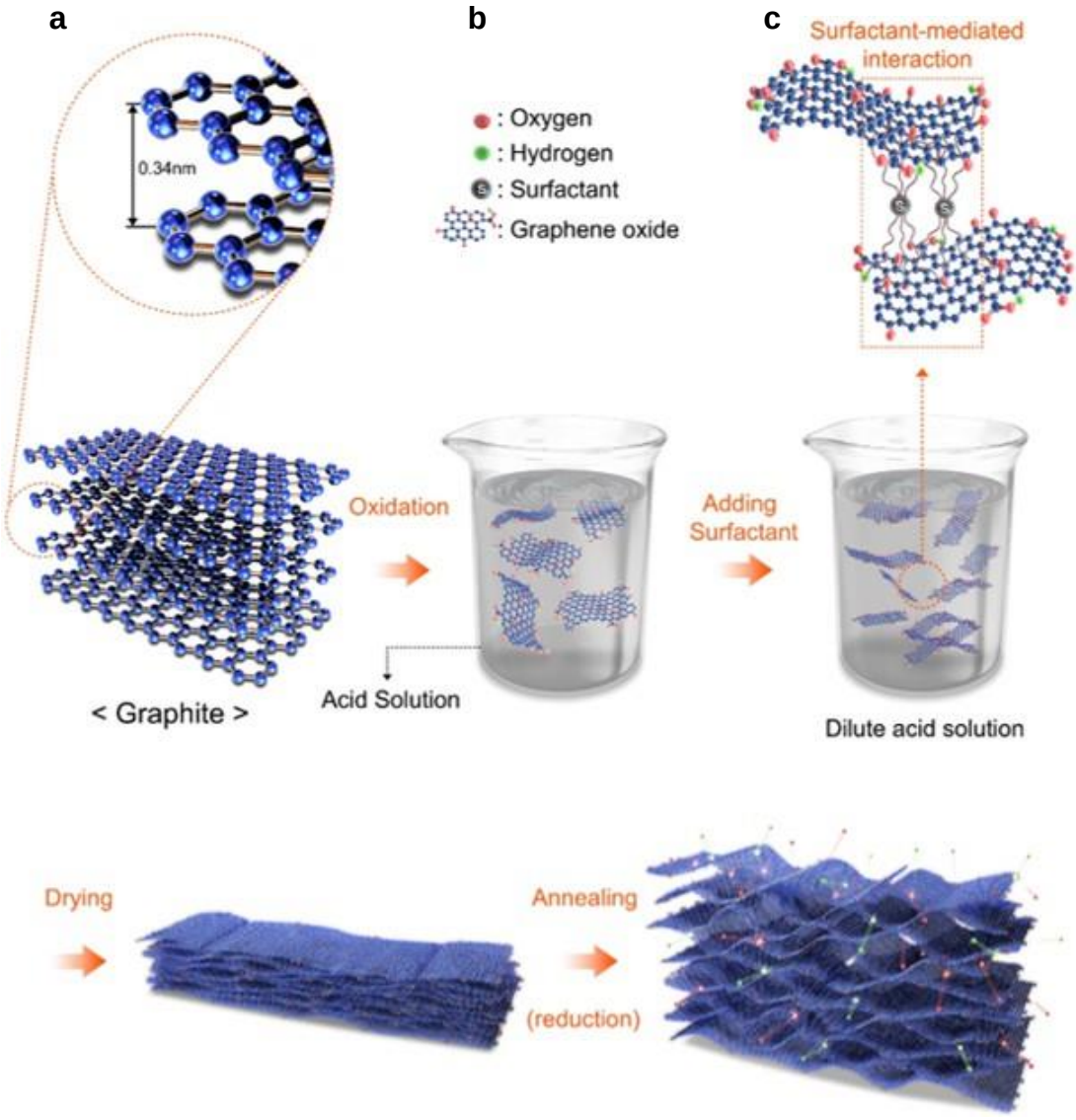

Figure 1. Schematic overview of the synthesis process for the self–assembly of reduced graphene nanosheets with a nanohoneycomb structure produced from bulk graphite flakes (+50 meshes). (a) Schematic representation of graphite with an interlayer spacing of 0.34 nm and (b) GO nanosheets obtained using a modified Hummers method. (c) Interactions between the GO functional groups and the surfactant, resulting in the attachment of graphene nanosheets at the atomic scale. (d) Thermal reduction of GO, resulting in a volume expansion of the compacted nanohoneycomb–like structure.

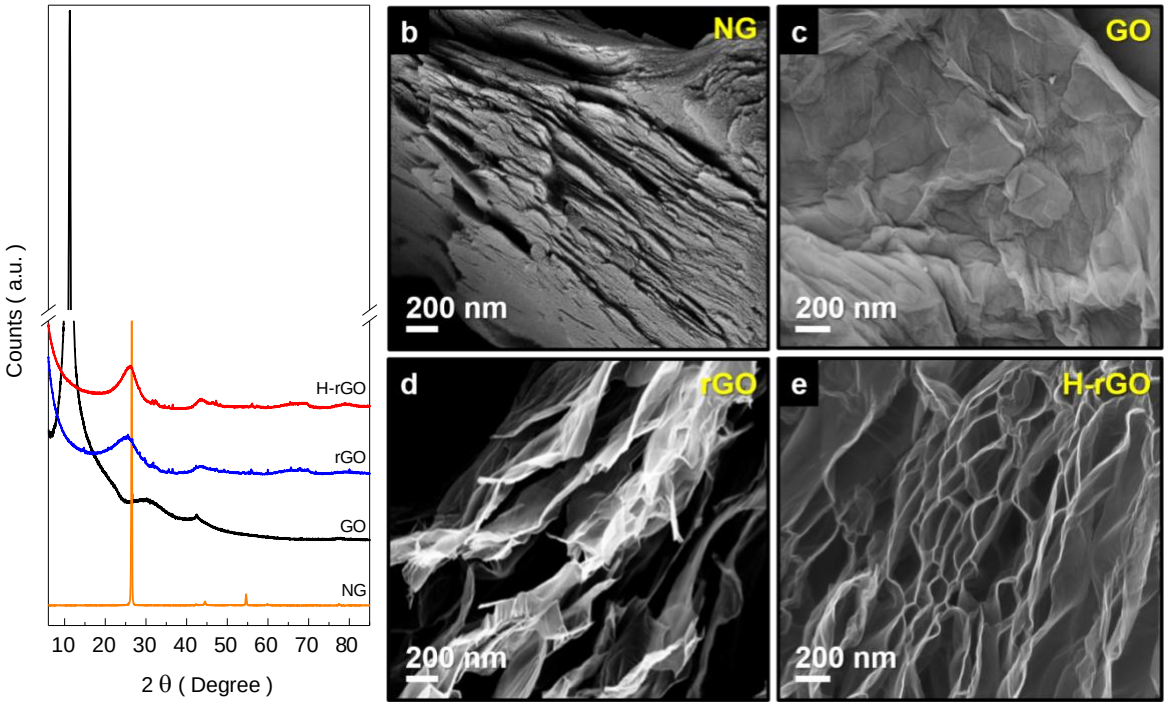

Figure 2. (a) Comparative HR–XRD spectra of the graphite and graphene phases used to obtain the unique nanohoneycomb–like structure. FESEM images of (b) NG, (c) GO, (d) rGO, and (e) H-rGO powder samples.

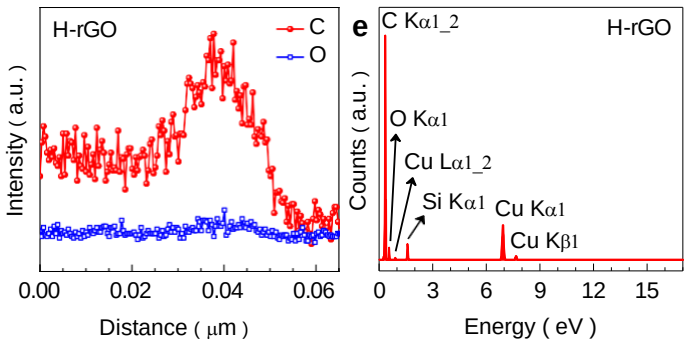

Figure 3. (a) TEM and (b) HRTEM images of H-rGO. The TEM image reveals the microscopic textural properties of the nanohoneycomb–like graphene structure and the interconnected corrugated layered morphology. The HRTEM image reveals that the graphene layers are integrated at the merging sites, leading to the coexistence of graphite/graphene allotropes in the convergence/divergence regions. The magnified HRTEM image shows interplanar lattice spacings of 3.4 ± 1 and 2.1 ± 1 Å corresponding to the reflections of the graphite (002) and (100) planes (JCPDS card no. 75−1621), respectively, as well as interplanar lattice spacings of 3.2 ± 1 and 7.1 ± 1 Å corresponding to the reflection of the graphene (222) and (111) planes (JCPDS card no. 49−1717), respectively. (c) SAED ring pattern of the reflections of the graphite (002) and (102) planes and the graphene (420), (311), and (200) planes. (d) Elemental line–scan profile showing the large amount of carbon (the red dotted line) and the small amount of oxygen (the blue dotted line), which is consistent with (e) the EDS results. (f) EDS–STEM electron image, overlay image, and individual mapping images revealing a uniform distribution of the C and O.

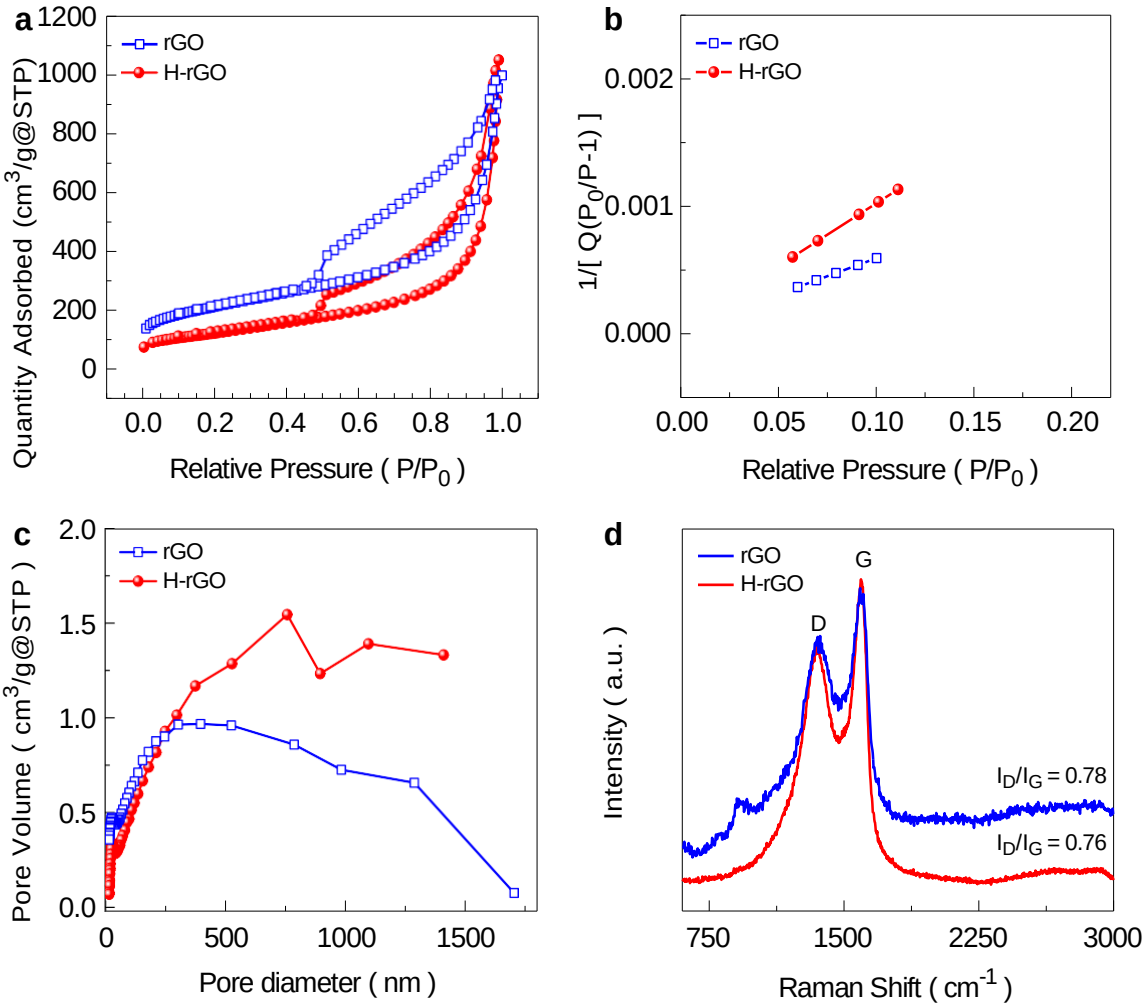

Figure 4. (a) N_2 adsorption−desorption isotherm curves, b) BET specific surface area, (c) pore–diameter distribution, and (d) Raman spectra of the rGO and H-rGO samples.

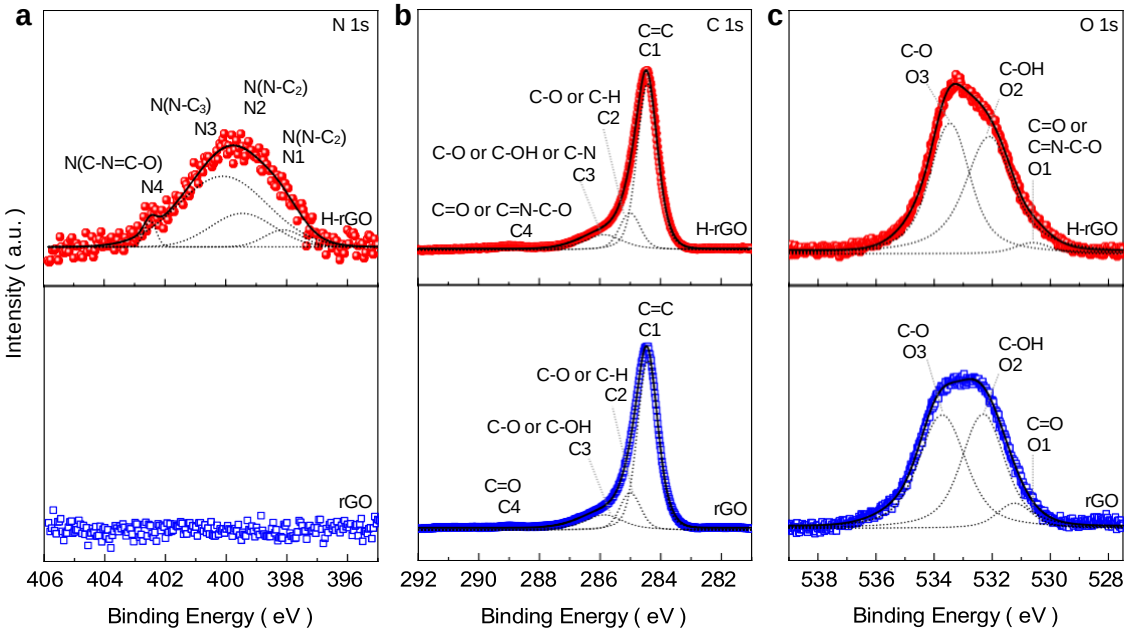

Figure 5. HRPES spectra of (a) N 1s, (b) C 1s, and (c) O 1s for the rGO and H-rGO samples. The HRPES spectra were deconvoluted using a Gaussian curve fitting model. Of the constituents, the C1s was dominant over the O 1s. In particular, only the H-rGO exhibits the presence of nitrogen in its graphene structure.

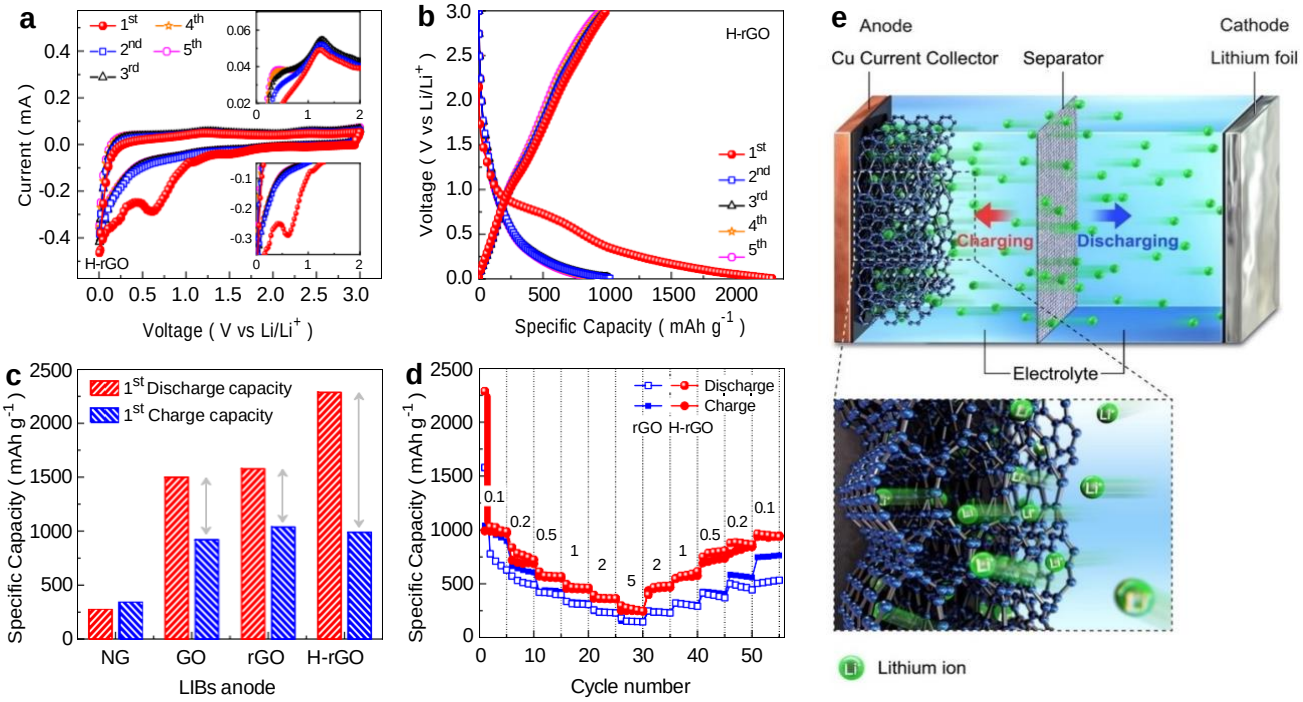

Figure 6. Initial five (a) CV sweeps and (b) galvanostatic discharge/charge profiles of the rGO and H-rGO anodes. The CV measurements were performed at 0.1 mV s^{-1}, whereas the discharge/charge curves were recorded at a current of 0.1 A g^{-1}. (c) First–cycle discharge/charge capacities and (d) restoration performance of the NG, GO, rGO, and H-rGO anodes. (e) Schematic representation of the operating mechanisms for an LIB during the lithiation–delithiation process in a typical battery cell with H-rGO as the anode, a separator, Li–foil as the cathode, and $LiPF_6$ as the electrolyte with EC/DEC (1:1 v/v; sky–blue region). The green solid spheres represent the Li–ions. The Li–ions migrate towards and away from nanohoneycomb graphene during the lithiation–delithiation processes, respectively. The magnified image illustrates the lithiation of Li–ions near the surface of the nanohoneycomb–like graphene.

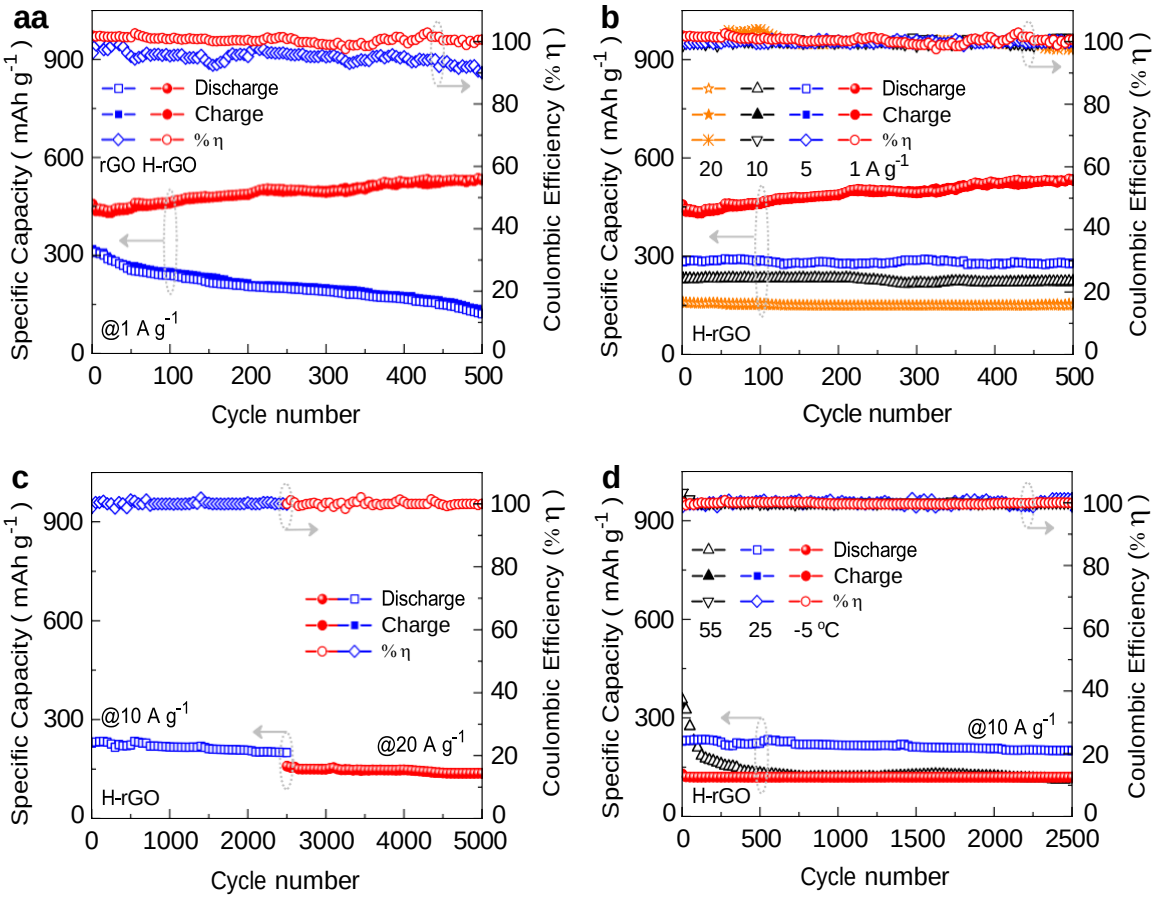

Figure 7. (a) Long–term cycling durability of the rGO and H-rGO anodes at a moderate current of 1.0 A g^{-1} over 500 lithiation–delithiation cycles. (b) Long–term cycling stability of the H-rGO anode at various current densities up to 20 A g^{-1} for 500 lithiation–delithiation cycles. (c) Ultra–long lithiation–delithiation stability curves of the H-rGO anode recorded at very high current densities of 10 and 20 A g^{-1}. (d) Stability performance of the H-rGO anode measured at a high current density of 10 A g^{-1} for 2,500 continuous lithiation–delithiation cycles.

References

[1] T. Or, S.W.D. Gourley, K. Kaliyappan, A. Yu, Z. Chen, Recycling of mixed cathode lithium-ion batteries for electric vehicles: Current status and future outlook, Carbon Energy, 2 (2020) 6-43.

[2] W. Mrozik, M.A. Rajaeifar, O. Heidrich, P. Christensen, Environmental impacts, pollution sources and pathways of spent lithium-ion batteries, Energy Environ. Sci., 14

(2021) 6099-6121.

[3] X. Wu, K. Song, X. Zhang, N. Hu, L. Li, W. Li, L. Zhang, H. Zhang, Safety Issues in Lithium Ion Batteries: Materials and Cell Design, Front. Energy Res., 7 (2019).

[4] S. Cho, J.C. Hyun, S. Ha, Y. Choi, H. Seong, J. Choi, H.-J. Jin, Y.S. Yun, Sulfur-doped hard carbon hybrid anodes with dual lithium-ion/metal storage bifunctionality for high-energy-density lithium-ion batteries, Carbon Energy, 5 (2023) e288.

[5] Z. Huang, Z. Deng, Y. Zhong, M. Xu, S. Li, X. Liu, Y. Zhou, K. Huang, Y. Shen, Y. Huang, Progress and challenges of prelithiation technology for lithium-ion battery, Carbon Energy, 4 (2022) 1107-1132.

[6] H. Chen, M. Zheng, S. Qian, H.Y. Ling, Z. Wu, X. Liu, C. Yan, S. Zhang, Functional additives for solid polymer electrolytes in flexible and high-energy-density solid-state lithium-ion batteries, Carbon Energy, 3 (2021) 929-956.

[7] A.T.A. Ahmed, B. Hou, A.I. Inamdar, S. Cha, H. Kim, H. Im, Morphology Engineering of Self-Assembled Nanostructured $CuCo_2O_4$ Anodes for Lithium-Ion Batteries, Energy Technol-Ger, 7 (2019) 1900295.

[8] A.T.A. Ahmed, R. Soni, A.S. Ansari, C.Y. Lee, H.-S. Kim, H. Im, C. Bathula, Biowaste-derived graphitic carbon interfaced TiO_2 as anode for lithium-ion battery, Surfaces and Interfaces, 35 (2022) 102404.

[9] A.I. Inamdar, A.S. Salunke, B. Hou, N.K. Shrestha, H. Im, H. Kim, Highly durable and sustainable copper–iron–tin–sulphide (Cu_2FeSnS_4) anode for Li-ion batteries: effect of operating temperatures, Dalton Trans., 52 (2023) 12020-12029.

[10] J.R. Dahn, A.K. Sleigh, H. Shi, J.N. Reimers, Q. Zhong, B.M. Way, Dependence of the electrochemical intercalation of lithium in carbons on the crystal structure of the carbon, Electrochim. Acta, 38 (1993) 1179-1191.

[11] A.L.M. Reddy, A. Srivastava, S.R. Gowda, H. Gullapalli, M. Dubey, P.M. Ajayan, Synthesis Of Nitrogen-Doped Graphene Films For Lithium Battery Application, ACS Nano, 4 (2010) 6337-6342.

[12] P. Lian, X. Zhu, S. Liang, Z. Li, W. Yang, H. Wang, Large reversible capacity of high quality graphene sheets as an anode material for lithium-ion batteries, Electrochim. Acta, 55 (2010) 3909-3914.

[13] W. Eom, E. Lee, S.H. Lee, T.H. Sung, A.J. Clancy, W.J. Lee, T.H. Han, Carbon nanotube-reduced graphene oxide fiber with high torsional strength from rheological hierarchy control, Nat. Commun., 12 (2021) 396.

[14] F. Guo, M. Creighton, Y. Chen, R. Hurt, I. Külaots, Porous structures in stacked, crumpled and pillared graphene-based 3D materials, Carbon, 66 (2014) 476-484.

[15] S. Abouali, M.A. Garakani, L. Silvestri, E. Venezia, L. Marasco, R. Brescia, A. Ansaldo, M. Serri, J.K. Panda, G. Pugliese, E. Mantero, F. Bonaccorso, V. Pellegrini, From scaled-up production of silicon-graphene nanocomposite to the realization of an ultra-stable full-cell Li-ion battery, 2D Mater., 8 (2021) 035014.

[16] J.R. Dahn, T. Zheng, Y. Liu, J.S. Xue, Mechanisms for Lithium Insertion in Carbonaceous Materials, Sci. Reports, 270 (1995) 590-593.

[17] Y. Liu, J.S. Xue, T. Zheng, J.R. Dahn, Mechanism of lithium insertion in hard carbons prepared by pyrolysis of epoxy resins, Carbon, 34 (1996) 193-200.

[18] R. Raccichini, A. Varzi, S. Passerini, B. Scrosati, The role of graphene for electrochemical energy storage, Nat. Mater., 14 (2015) 271-279.

[19] Q. Cheng, Y. Okamoto, N. Tamura, M. Tsuji, S. Maruyama, Y. Matsuo, Graphene-Like-Graphite as Fast-Chargeable and High-Capacity Anode Materials for Lithium Ion Batteries, Sci. Reports, 7 (2017) 14782.

[20] H. Sun, A. Varzi, V. Pellegrini, D.A. Dinh, R. Raccichini, A.E. Del Rio-Castillo, M. Prato, M. Colombo, R. Cingolani, B. Scrosati, S. Passerini, F. Bonaccorso, How much does size really matter? Exploring the limits of graphene as Li ion battery anode material, Solid State Commun., 251 (2017) 88-93.

[21] C.-A. Tseng, C.-P. Lee, Y.-J. Huang, H.-W. Pang, K.-C. Ho, Y.-T. Chen, One-step synthesis of graphene hollow nanoballs with various nitrogen-doped states for electrocatalysis in dye-sensitized solar cells, Mater. Today Energy, 8 (2018) 15-21.

[22] D.H. Youn, S.K. Stauffer, P. Xiao, H. Park, Y. Nam, A. Dolocan, G. Henkelman, A. Heller, C.B. Mullins, Simple Synthesis of Nanocrystalline Tin Sulfide/N-Doped Reduced Graphene Oxide Composites as Lithium Ion Battery Anodes, ACS Nano, 10 (2016) 10778-10788.

[23] X. Zhu, Y. Zhu, S. Murali, M.D. Stoller, R.S. Ruoff, Nanostructured Reduced Graphene Oxide/Fe_2O_3 Composite As a High-Performance Anode Material for Lithium Ion Batteries, ACS Nano, 5 (2011) 3333-3338.

[24] L. Luo, J. Wu, J. Luo, J. Huang, V.P. Dravid, Dynamics of Electrochemical Lithiation/Delithiation of Graphene-Encapsulated Silicon Nanoparticles Studied by In-situ TEM, Sci. Reports, 4 (2014) 3863.

[25] P. Sehrawat, A. Abid, S.S. Islam, A. Mauger, C.M. Julien, Nanostructured Graphene Oxide-Based Hybrids as Anodes for Lithium-Ion Batteries, C, 6 (2020) 81.

[26] I.H. Son, J.H. Park, S. Park, K. Park, S. Han, J. Shin, S.-G. Doo, Y. Hwang, H. Chang, J.W. Choi, Graphene balls for lithium rechargeable batteries with fast charging and high volumetric energy densities, Nat. Commun., 8 (2017) 1561.

[27] Q. Liu, Z.-F. Li, Y. Liu, H. Zhang, Y. Ren, C.-J. Sun, W. Lu, Y. Zhou, L. Stanciu, E.A. Stach, J. Xie, Graphene-modified nanostructured vanadium pentoxide hybrids with extraordinary electrochemical performance for Li-ion batteries, Nat. Commun., 6 (2015) 6127.

[28] C. Liu, T. Zhang, L. Cao, K. Luo, High-Capacity Anode Material for Lithium-Ion Batteries with a Core–Shell $NiFe_2O_4$/Reduced Graphene Oxide Heterostructure, ACS Omega, 6 (2021) 25269-25276.

[29] L. Zhang, J. Liu, D. Xiao, Y. Chen, S. Zhang, L. Yan, X. Gu, X. Zhao, Reduced Graphene Oxide Modulated FeSe/C Anode Materials for High-Stable and Long-Life Potassium-Ion Batteries, Chem. – Eur. J., 29 (2023) e202302811.

[30] K. Ullah, N. Shah, R. Wadood, B.M. Khan, W.C. Oh, Recent trends in graphene based transition metal oxides as anode materials for rechargeable lithium-ion batteries, Nano Trends, 1 (2023) 100004.

[31] S. Yu, B. Guo, T. Zeng, H. Qu, J. Yang, J. Bai, Graphene-based lithium-ion battery anode materials manufactured by mechanochemical ball milling process: A review and perspective, Compos. B. Eng., 246 (2022) 110232.

[32] P.K. T. K. M, D. Tripathy, H. Aiyer, S. Sampath, A Ternary Metal Oxide-Reduced Graphene Oxide Composite as High Capacity and Durable Anode for Li-Ion Batteries, J. Electrochem. Soc., 170 (2023) 080526.

[33] T. Hu, X. Sun, H. Sun, G. Xin, D. Shao, C. Liu, J. Lian, Rapid synthesis of nitrogen-doped graphene for a lithium ion battery anode with excellent rate performance and super-long cyclic stability, Phys. Chem. Chem. Phys., 16 (2014) 1060-1066.

[34] P. Guo, H. Song, X. Chen, Electrochemical performance of graphene nanosheets as anode material for lithium-ion batteries, Electrochem. Commun., 11 (2009) 1320-1324.

[35] J.M. Tarascon, M. Armand, Issues and challenges facing rechargeable lithium batteries, Nat. , 414 (2001) 359-367.

[36] Z. Yu, J. Song, M.L. Gordin, R. Yi, D. Tang, D. Wang, Phosphorus-Graphene Nanosheet Hybrids as Lithium-Ion Anode with Exceptional High-Temperature Cycling Stability, Adv. Sci., 2 (2015) 1400020.

[37] M. Lu, S. Liu, J. Chen, X. Zhang, J. Zhang, Z. Li, B. Hou, Rational-Designed Hybrid Aerogels for Ultra-Flyweight Electrochemical Energy Storage, J. Phys. Chem. C, 124 (2020) 15688-15697.

[38] M. Lu, G. Wang, B. Li, J. Chen, J. Zhang, Z. Li, B. Hou, Molecular interaction balanced one- and two-dimensional hybrid nanoarchitectures for high-performance supercapacitors, Phys. Chem. Chem. Phys., 21 (2019) 22283-22292.

[39] A.T.A. Ahmed, B. Hou, S.M. Pawar, H. Kim, H. Im, Graphene-integrated $CuCo_2S_4$ microspheres as a sustainable anode material for high-performance Li-ion batteries, Int. J. Energy Res., 45 (2021) 1613-1626.

[40] Z. Yan, H. Jin, J. Guo, Low-temperature synthesis of graphitic carbon-coated silicon anode materials, Carbon Energy, 1 (2019) 246-252.

[41] B.E. Warren, X-Ray Diffraction in Random Layer Lattices, Phys. Rev., 59 (1941) 693-698.

[42] B. Hou, D. Parker, G.P. Kissling, J.A. Jones, D. Cherns, D.J. Fermín, Structure and Band Edge Energy of Highly Luminescent $CdSe_{1-x}Tex$ Alloyed Quantum Dots, J. Phys. Chem. C, 117 (2013) 6814-6820.

[43] T.K. Shruthi, M.S. Kumar, M. Arjunan, A. Pratap, N. Chandrasekaran, Graphene oxide aided structural tailoring of 3-D N-doped amorphous carbon network for enhanced energy storage, RSC Adv., 5 (2015) 93423-93432.

[44] G. Leofanti, M. Padovan, G. Tozzola, B. Venturelli, Surface area and pore texture of catalysts, Catal. Today, 41 (1998) 207-219.

[45] S. Gadipelli, Z.X. Guo, Graphene-based materials: Synthesis and gas sorption, storage and separation, Prog. Mater. Sci., 69 (2015) 1-60.

[46] Z. Xing, Z. Ju, Y. Zhao, J. Wan, Y. Zhu, Y. Qiang, Y. Qian, One-pot hydrothermal synthesis of Nitrogen-doped graphene as high-performance anode materials for lithium ion batteries, Sci. Reports, 6 (2016) 26146.

[47] T.M. Paronyan, A.K. Thapa, A. Sherehiy, J.B. Jasinski, J.S.D. Jangam, Incommensurate Graphene Foam as a High Capacity Lithium Intercalation Anode, Sci. Reports, 7 (2017) 39944.

[48] T. Susi, T. Pichler, P. Ayala, X-ray photoelectron spectroscopy of graphitic carbon nanomaterials doped with heteroatoms, Beilstein J. Nanotechnol., 6 (2015) 177-192.

[49] D. Long, W. Li, L. Ling, J. Miyawaki, I. Mochida, S.-H. Yoon, Preparation of Nitrogen-Doped Graphene Sheets by a Combined Chemical and Hydrothermal Reduction of Graphene Oxide, Langmuir, 26 (2010) 16096-16102.

[50] Y.-C. Lin, C.-Y. Lin, P.-W. Chiu, Controllable graphene N-doping with ammonia plasma, Appl. Phys. Lett., 96 (2010) 133110.

[51] Z.-H. Sheng, L. Shao, J.-J. Chen, W.-J. Bao, F.-B. Wang, X.-H. Xia, Catalyst-Free Synthesis of Nitrogen-Doped Graphene via Thermal Annealing Graphite Oxide with Melamine and Its Excellent Electrocatalysis, ACS Nano, 5 (2011) 4350-4358.

[52] H.J. Kim, I.-S. Bae, S.-J. Cho, J.-H. Boo, B.-C. Lee, J. Heo, I. Chung, B. Hong,

Synthesis and characteristics of NH_2-functionalized polymer films to align and immobilize DNA molecules, Nanoscale Res. Lett., 7 (2012) 30.

[53] L. Tian, Q. Zhuang, J. Li, Y. Shi, J. Chen, F. Lu, S. Sun, Mechanism of intercalation and deintercalation of lithium ions in graphene nanosheets, Chin. Sci. Bull., 56 (2011) 3204.

[54] J. Zhang, Z. Xie, W. Li, S. Dong, M. Qu, High-capacity graphene oxide/graphite/carbon nanotube composites for use in Li-ion battery anodes, Carbon, 74 (2014) 153-162.

[55] G. Wang, X. Shen, J. Yao, J. Park, Graphene nanosheets for enhanced lithium storage in lithium ion batteries, Carbon, 47 (2009) 2049-2053.

[56] A. Ganguly, S. Sharma, P. Papakonstantinou, J. Hamilton, Probing the Thermal Deoxygenation of Graphene Oxide Using High-Resolution In Situ X-ray-Based Spectroscopies, J. Phys. Chem. C, 115 (2011) 17009-17019.

[57] Y.-C. Chiang, C.-C. Liang, C.-P. Chung, Characterization of Platinum Nanoparticles Deposited on Functionalized Graphene Sheets, Mater. , 8 (2015) 6484-6497.

[58] Y. Zhang, Z. Sun, H. Wang, Y. Wang, M. Liang, S. Xue, Nitrogen-doped graphene as a cathode material for dye-sensitized solar cells: effects of hydrothermal reaction and annealing on electrocatalytic performance, RSC Adv., 5 (2015) 10430-10439.

[59] Z.-S. Wu, W. Ren, L. Xu, F. Li, H.-M. Cheng, Doped Graphene Sheets As Anode Materials with Superhigh Rate and Large Capacity for Lithium Ion Batteries, ACS Nano, 5 (2011) 5463-5471.

[60] Y. Sun, J. Tang, K. Zhang, J. Yuan, J. Li, D.-M. Zhu, K. Ozawa, L.-C. Qin, Comparison of reduction products from graphite oxide and graphene oxide for anode applications in lithium-ion batteries and sodium-ion batteries, Nanoscale, 9 (2017) 2585-2595.

[61] Y. Tang, J. Chen, Z. Mao, C. Roth, D. Wang, Highly N-doped carbon with low graphitic-N content as anode material for enhanced initial Coulombic efficiency of lithium-ion batteries, Carbon Energy, 5 (2023) e257.

[62] B. Huang, Y. Huang, Z. Wang, L. Chen, R. Xue, F. Wang, Characteristics of pyrolyzed phenol-formaldehyde resin as an anode for lithium-ion batteries, J. Power Sources, 58 (1996) 231-234.

[63] J.S. Xue, J.R. Dahn, Dramatic Effect of Oxidation on Lithium Insertion in Carbons Made from Epoxy Resins, J. Electrochem. Soc., 142 (1995) 3668.

[64] E. Yoo, J. Kim, E. Hosono, H.-s. Zhou, T. Kudo, I. Honma, Large Reversible Li

Storage of Graphene Nanosheet Families for Use in Rechargeable Lithium Ion Batteries, Nano Lett., 8 (2008) 2277-2282.

[65] S.S. Zhang, K. Xu, T.R. Jow, Electrochemical impedance study on the low temperature of Li-ion batteries, Electrochim. Acta, 49 (2004) 1057-1061.

[66] S.S. Zhang, K. Xu, T.R. Jow, A new approach toward improved low temperature performance of Li-ion battery, Electrochem. Commun., 4 (2002) 928-932.

[67] S.S. Zhang, K. Xu, T.R. Jow, The low temperature performance of Li-ion batteries, J. Power Sources, 115 (2003) 137-140.

[68] W. Song, M. Chen, F. Bai, S. Lin, Y. Chen, Z. Feng, Non-uniform effect on the thermal/aging performance of Lithium-ion pouch battery, Appl. Therm. Eng., 128 (2018) 1165-1174.